

BIOCHEMISTRY

Mechanisms of KCNQ1 channel dysfunction in long QT syndrome involving voltage sensor domain mutations

Hui Huang,^{1,2} Georg Kuenze,^{2,3,4} Jarrod A. Smith,^{1,2} Keenan C. Taylor,^{1,2} Amanda M. Duran,^{2,3,4} Arina Hadziselimovic,^{1,2} Jens Meiler,^{2,3,4,5} Carlos G. Vanoye,⁶ Alfred L. George Jr.,⁶ Charles R. Sanders^{1,2,7*}

Mutations that induce loss of function (LOF) or dysfunction of the human KCNQ1 channel are responsible for susceptibility to a life-threatening heart rhythm disorder, the congenital long QT syndrome (LQTS). Hundreds of *KCNQ1* mutations have been identified, but the molecular mechanisms responsible for impaired function are poorly understood. We investigated the impact of 51 *KCNQ1* variants with mutations located within the voltage sensor domain (VSD), with an emphasis on elucidating effects on cell surface expression, protein folding, and structure. For each variant, the efficiency of trafficking to the plasma membrane, the impact of proteasome inhibition, and protein stability were assayed. The results of these experiments combined with channel functional data provided the basis for classifying each mutation into one of six mechanistic categories, highlighting heterogeneity in the mechanisms resulting in channel dysfunction or LOF. More than half of the *KCNQ1* LOF mutations examined were seen to destabilize the structure of the VSD, generally accompanied by mistrafficking and degradation by the proteasome, an observation that underscores the growing appreciation that mutation-induced destabilization of membrane proteins may be a common human disease mechanism. Finally, we observed that five of the folding-defective LQTS mutant sites are located in the VSD S0 helix, where they interact with a number of other LOF mutation sites in other segments of the VSD. These observations reveal a critical role for the S0 helix as a central scaffold to help organize and stabilize the *KCNQ1* VSD and, most likely, the corresponding domain of many other ion channels.

INTRODUCTION

The *KCNQ1* (Kv7.1) voltage-gated potassium channel contributes to a variety of physiological processes, most notably when it complexes with the *KCNE1* accessory protein to generate the slow delayed rectifier current (I_{Ks}) of the cardiac action potential (1–6). Heritable mutations in *KCNQ1* resulting in channel dysfunction or loss of function (LOF) lead to type 1 long QT syndrome (LQTS), a potentially life-threatening predisposition to cardiac arrhythmia (6, 7). However, many patients with LQTS are unaware of their condition.

More than 600 *KCNQ1* mutations associated with LQTS have been identified, and this number continues to grow (8–10). Although progress in functional characterization of LQTS-associated *KCNQ1* mutations has been made (11–16), the mechanistic basis of channel dysfunction for most mutations is not known. Moreover, the expanding use of exome/genome sequencing contributes to a growing database of unclassified human *KCNQ1* mutations. These “variants of unknown significance” (VUS) present a medical quandary in the context of genetic testing for LQTS and the medical decision of who to preemptively treat with invasive procedures such as implantation of a defibrillator (17). The dearth of direct experimental data to determine how mutations alter channel function has prompted bioinformatic and modeling efforts to predict pathogenicity (16, 18–20). However, results from these *in silico* approaches are not considered strong evidence by genetic testing standards established by the American College of Medical Genetics

and Genomics (ACMG) (21). This is in contrast to *in vitro* experimental data documenting mutation-induced LOF for a disease-linked protein, which the ACMG guidelines categorize as strong evidence for pathogenicity (21).

Here, we assess medium-throughput experimental studies of *KCNQ1* variants as a route to assessing their functional and biochemical consequences and determining the mechanistic basis for pathogenicity. A set of 51 single-site mutants affecting sites located in the *KCNQ1* voltage sensor domain (VSD) was compared to the wild-type (WT) channel. A cross section of mutants was selected to represent three classes of variants: known LQTS mutations, documented human VUS, and mutations predicted to be neutral based on WT occurrence within nonhuman *KCNQ1* orthologs. The results of this work implicate the underlying mechanisms for LQTS-associated LOF mutations and also support the notion that most of the examined VUS are deleterious. Moreover, analysis of mutations that affect amino acid sites that are located in the VSD S0 segment or that directly interact with S0 provides evidence that this overlooked structural element is critical for channel stability and function.

RESULTS

Structure mapping of 51 human *KCNQ1* variants

The *KCNQ1* mutations chosen for this study represent three groups: (i) 17 previously associated with LQTS, (ii) 21 human VUS for which there have been insufficient data for classification as benign or pathogenic, and (iii) 13 designed variants predicted to be benign. The predicted benign variants were based on swapping in an amino acid observed to be divergent from the WT sequence in a nonhuman ortholog of *KCNQ1* (22). For example, site 104 in human *KCNQ1* is a threonine but is serine at the corresponding site in chameleon and finch *KCNQ1*. The T104S mutation is therefore predicted to exhibit no significant functional consequences. All mutations are in the VSD and include many known

¹Department of Biochemistry, Vanderbilt University, Nashville, TN 37240, USA.

²Center for Structural Biology, Vanderbilt University, Nashville, TN 37240, USA.

³Department of Chemistry, Vanderbilt University, Nashville, TN 37235, USA.

⁴Department of Pharmacology, Vanderbilt University, Nashville, TN 37240, USA.

⁵Department of Bioinformatics, Vanderbilt University Medical Center, Nashville, TN 37232, USA.

⁶Department of Pharmacology, Northwestern University Feinberg School of Medicine, Chicago, IL 60611, USA.

⁷Department of Medicine, Vanderbilt University Medical Center, Nashville, TN 37232, USA.

*Corresponding author. Email: chuck.sanders@vanderbilt.edu

single-residue LQTS mutations in the S0 and S1 segments (fig. S1A). Figure S1 (B and C) shows their locations in the recently determined structure of the voltage sensor of *Xenopus laevis* KCNQ1 (23). Although the present study was carried out using human KCNQ1, high homology indicates that the *Xenopus* structure can be assumed to be an excellent model for human KCNQ1. As shown in fig. S1, a majority of the mutations examined in this work (whether surface-exposed or buried) are located in the cytosol-facing half of the VSD, although mutations in the ectoplasm-facing half are also included.

As described elsewhere (22) and summarized in table S1, each of the 51 mutants was coexpressed in Chinese hamster ovary (CHO)–K1 cells with WT human KCNE1 and functionally characterized using whole-cell electrophysiology (EP) to assess the effect of each mutation on K⁺ current amplitude, on voltage dependence of activation, and on deactivation kinetics. The EP data identified 32 KCNQ1 mutants that failed to yield at least 65% of peak WT K⁺ channel current and were therefore classified as LOF. The 65% value chosen for the cutoff for effective LOF is based on the approximate boundary between the range of currents observed for known LQTS mutants and benign mutants based on an extensive literature review [see also the study of Li *et al.* (16)]. The underlying mechanisms for LOF in these 32 mutants were not established by the functional data alone, leading to the experiments of the present study.

Mistrafficking as a common cause of mutation-induced channel LOF

We developed a method for quantitating KCNQ1 cell surface and total expression. Using a fully functional form of KCNQ1 in which a Myc epitope is inserted into the extracellular loop connecting S1 and S2 (24), we transiently expressed WT and variant channels in human embryonic kidney (HEK) 293 cells, followed by labeling the cell surface population of KCNQ1 with an anti-Myc antibody conjugated to phycoerythrin (PE). The cells were then permeabilized, and the intracellular population of KCNQ1 was labeled with a second anti-Myc antibody, this time conjugated with Alexa Fluor 647. The cells were then subjected to flow cytometry to measure the single-cell intensities of PE and Alexa Fluor 647 fluorescence, providing quantification of both total and surface channel expression levels (fig. S2). Figure 1A shows the quantified cell surface levels for KCNQ1 mutants and reveals that many LQTS and VUS mutants exhibit much lower surface expression than WT. In considering these results, we acknowledge that HEK293 cells are an imperfect replacement for cardiomyocytes or CHO-K1 cells (optimal for functional studies of KCNQ1). However, the use of cardiomyocytes for high- or medium-throughput EP and trafficking experiments of KCNQ1 mutants cotransfected with KCNE1 is not currently feasible. Moreover, we found that HEK293 cells yielded higher signal-to-noise measurements in our trafficking assays than CHO-K1. Fortunately, as will be shown, the use of HEK293 cells yielded results that are strikingly consistent with what is expected based on the previous EP results, disease classification, and predictions for this panel of 51 KCNQ1 variants.

Figure 1A also shows that there is a strong correlation between cell surface expression levels and total (surface + internal) expression. This correlation can be explained on the basis of two factors. First, mutant KCNQ1 channels exhibit lower cell surface expression levels because of reduced total expression. Second, for many mutants exhibiting low total expression, it was seen that surface expression is even lower than predicted on the basis of the fractional degree of reduction seen for total expression. A replot of the data is shown in Fig. 1B, which illustrates the relative contributions of these two factors: This panel shows the surface trafficking efficiency versus total expression, where efficiency is defined

as (cell surface)/(total) levels for the mutant relative to (cell surface)/(total) levels for WT ($\times 100$). It is seen that 18 of the 23 mutants exhibiting $\leq 65\%$ of total WT expression also exhibit cell surface trafficking efficiencies that are $\leq 65\%$ that of WT. This not only indicates that some mutants exhibit low total expression but also suggests that, in such cases, the modest population of channel that does express is surface trafficking-impaired. There are also a number of mutants with moderate [for example, L134P ($60 \pm 3\%$ relative to WT)] or low total expression levels [for example, R174L ($18 \pm 2\%$ relative to WT)] that exhibit surface trafficking efficiencies that are much higher than expected ($178 \pm 12\%$ for L134P and $68 \pm 8\%$ for R174L), indicating exceptions to the general correlation between total expression levels and surface trafficking efficiency. We also note the gratifying result that all 13 predicted benign mutants exhibited both total and surface expression levels that are similar to WT.

Figure 1C and table S1 present peak channel current densities for each mutant (22) juxtaposed with the cell surface expression levels. This reveals that channel function and surface trafficking are often strongly coupled, indicating that reduced levels of KCNQ1 at the plasma membrane are the most common contributing factor to channel LOF for the mutants examined in this work. Figure S3 further clarifies this correlation by showing that a majority of the mutants exhibiting low current densities are also subject to low cell surface trafficking efficiency.

Because KCNQ1 in cardiac myocytes coassembles with the KCNE1 protein to form a complex early in the secretory pathway (25–27), we tested whether coexpression of KCNQ1 with KCNE1 alters trafficking. For the 16 mutants tested, coexpression with WT KCNE1 led to, at most, moderate changes in cell surface expression levels (fig. S4). This suggests that, for each of the other 35 KCNQ1 mutants, the presence of KCNE1 is likely to exert no more than a moderate impact on total channel expression or on surface trafficking, although the possibility of outliers cannot be excluded.

Proteasomal degradation as the basis for the reduced expression of many KCNQ1 variants

Both low cell surface expression and low surface trafficking efficiencies correlated with low total protein expression (Fig. 1, A and B, and table S1). We hypothesized that reduced total expression is due to degradation of nascent KCNQ1 via the endoplasmic reticulum-associated protein degradation (ERAD)/proteasome pathway (28). To test this, cells transfected with poorly expressing KCNQ1 mutants were treated for 20 hours with a proteasome inhibitor, MG132 (25 μ M). As seen in Fig. 2, inhibition of the proteasome led to only modest changes in surface expression but usually resulted in dramatically enhanced total expression levels for the tested mutants, although not for WT. These results implicate the endoplasmic reticulum (ER) protein folding quality control system and the coupled ERAD/proteasome pathway as the major determinant of the differences in total expression levels between WT and most trafficking-deficient KCNQ1 mutants. Mistrafficking-prone mutants are more efficiently targeted for degradation than WT and variants that traffic with near-WT efficiency.

Impact of coexpressing mutant and WT KCNQ1 on cell surface channel levels

Because of the dominant nature of type 1 LQTS and the heterozygous (WT/mutant) state of KCNQ1 patients, we examined the effect of coexpressing trafficking-defective mutants with WT channels on expression levels. As shown in Fig. 3, most of the tested mutants exert a partially dominant-negative effect on WT surface expression, with this

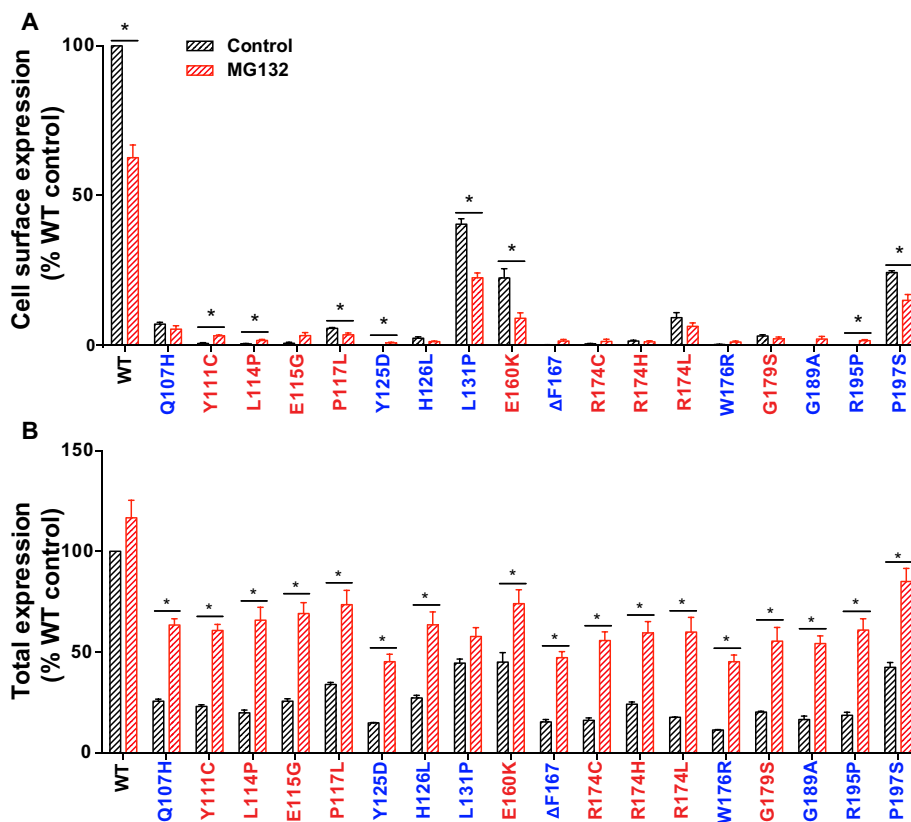


Fig. 2. Treatment of cells with a proteasome inhibitor (MG132) has modest impact on surface expression levels of the trafficking-deficient KCNQ1 variants (A) but often increases the total expression (B). Cells expressing WT or mutant KCNQ1 were treated with 25 μ M MG132 or vehicle for 20 hours. Cells were fixed and permeabilized (this step was omitted for measuring the surface expression) and then stained with myc-tag mouse monoclonal antibody. Cells were then washed and stained with anti-mouse Alexa Fluor 647 antibody. Immunostaining of 2500 cells was quantitated by flow cytometry. Results are expressed as mean \pm SEM for at least three independent experiments. Data are color-coded: LQTS mutant (red), VUS (blue), or predicted neutral polymorphism (black). Data labeled with an asterisk and a horizontal bar indicate those for which the measured KCNQ1 protein level for vehicle-treated cells was statistically different from the level measured in MG132-treated cells ($P < 0.05$).

by the ratio of WT/mutant subunits. These results indicate that although mutant-only expression assays are informative and yield data that correlate well with functional measurements (as in Fig. 1), additional insight can be gained by also conducting experiments under heterozygous conditions.

Use of NMR spectroscopy to identify severely folding-destabilized KCNQ1 variants

In an attempt to gain mechanistic insight into how mutations in KCNQ1 altered channel trafficking and function, we collected two-dimensional (2D) $^1\text{H}/^{15}\text{N}$ -TROSY (transverse relaxation optimized spectroscopy) NMR (nuclear magnetic resonance) spectra for WT and mutant forms of the VSD. TROSY spectra exhibit contour peaks for each amide $^1\text{H}/^{15}\text{N}$ pair along the protein backbone and provide a “fingerprint” pattern yielding insight into mutation-induced changes in protein structure and/or stability (29). The WT KCNQ1 VSD yields a well-resolved spectrum (Fig. 4A) in lyso-myristoylphosphatidylglycerol (LMPG) micelles, consistent with the protein being well folded. This spectrum was used as a reference for comparison with the spectra from 47 of the mutants examined in this work. Spectra were not acquired for the severely mistrafficking L114P, Δ F167, W176R, and R195P mutants because they failed to express to a sufficient level in *Escherichia coli* for the preparation of an NMR sample, consistent with the hypothesis that

they are severely unstable and/or misfolded, which is supported by additional data below.

Among the 47 mutants examined by NMR (Fig. 4, B to D, and fig. S5), two major classes of spectral changes were observed relative to the WT spectrum. First, all spectra exhibited some changes in peak positions (cf. Fig. 4B). These include differences for backbone amide peaks representing residues at or proximal to the mutation site. Shifts in peak positions for amides at some sequentially distal sites were also usually seen, which likely reflect minor distortion of tertiary structure and/or dynamics. There were no overt correlations between shifts in peak positions and either channel function or cell surface trafficking. Assessing the number of peaks that shift or the shift magnitudes also did not correlate with function and trafficking. This is not surprising given that ^1H and ^{15}N NMR chemical shifts are sensitive to many different factors and cannot readily be interpreted in conformational terms. We also found no evidence that shifts in peak position reflect a change in the equilibrium between two (possibly active and inactive) VSD states. We conclude that the differences in amide $^1\text{H}/^{15}\text{N}$ peak positions between these mutants and WT are not informative.

A second class of NMR spectral differences was observed for a subset of 13 mutants. These mutants yielded spectra in which many of the peaks were significantly broadened, in some cases to the point of complete disappearance. Examples are shown for moderate (Fig. 4C) and

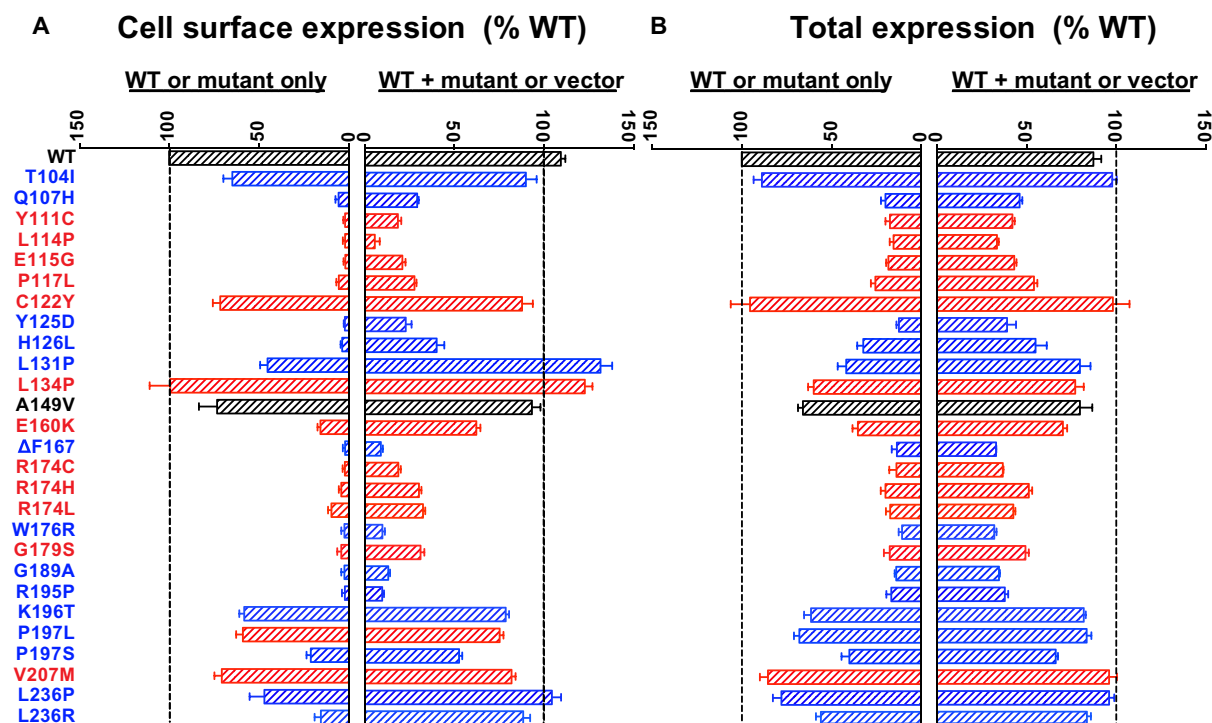


Fig. 3. Effect on KCNQ1 trafficking of coexpression of WT KCNQ1 with mutant KCNQ1. (A) Total WT + mutant expression levels and (B) surface WT + mutant expression levels. HEK293 cells were transiently transfected with either 0.5 μ g WT or mutant plasmid only (results on the left of each panel) or were cotransfected with both 0.25 μ g WT and 0.25 μ g mutant plasmids (heterozygous conditions, results presented on the right of each panel). See the legend of Fig. 1 for additional details.

severe (Fig. 4D) cases (see also fig. S5 and table S1). These results indicate mutation-induced destabilization of the folded state to an extent where there is an exchange of the protein between more than one conformational state. This exchange occurs at an intermediate rate on the NMR time scale, resulting in extensive line broadening for many peaks. The spectra of these 13 KCNQ1 mutants establish that the structures of these mutants are significantly destabilized relative to WT. The fact that this phenomenon is more severe for some mutants (see Fig. 4D) than others (for example, Fig. 4C) serves to identify the mutants that are most severely destabilized. It is notable that the 13 mutants showing moderate-to-severe peak broadening also exhibited loss of channel function and low total and surface expression levels (in all cases, <65% of WT values; see table S1). For these mutants, disease-associated LOF appears to stem from mutation-induced destabilization of the protein, resulting in impaired trafficking to the cell surface and enhanced degradation of the protein by the ERAD/proteasome pathway, a pathway it shares with HERG (human ether-à-go-go-related) potassium channel (30) and some other channels (31). These 13 mutants also tended to express more poorly in *E. coli* than trafficking-proficient mutants. Based on this, it is reasonable to assume that the four mutants that completely failed to express in *E. coli* are also severely folding-destabilized.

S0 as a central structural and dynamical element of the VSD

Five of the LQTS mutants in the little-characterized S0 segment were seen by NMR to be folding-defective (Q107, Y111C, L114P, E115G, and P117L) (red side chains in Fig. 5A). These and other LQTS sites in S0 directly interact with seven LQTS or VUS sites in S1 and S2 for which mutants are also mistrafficking-prone (Y125D, H126L, R174C, R174H, R174L, W176R, and G179S; magenta side chains in Fig. 5A). To further probe the interactions of S0 with the rest of the VSD, we con-

ducted molecular dynamics (MD) simulations on the VSD in an explicit 37°C 1,2-dimyristoyl-*sn*-glycero-3-phosphocholine (DMPC) bilayer. Three independent 500-ns MD runs were carried out, for a total of 1.5 μ s of simulation time. In each of these calculations, the VSD maintained its original structure and reached equilibrium after ca. 50 ns of simulation time (see fig. S6A). Analysis of the trajectories revealed a dense network of interactions of S0 with other parts of the VSD, as well as with water and lipids (Fig. 5B and fig. S6B). Important observed contacts that involve the LQTS and VUS sites are listed in table S2. The N-terminal half of S0 is bounded by the C-terminal end of S2 and involves π - π stacking between VUS mutation sites Q107 (S0) and W176 (S2) (Fig. 5C). The indole side chain of W176 also interacts with S0 hydrophobic residues V106 and V110 on one side and is exposed to lipid on the other side. The W176R mutation would eliminate the π - π interaction and also introduce a charged side chain adjacent to lipid. Similarly, residues in S2 (A178 and C180) and the S2-S3 linker (Y184 and F193) form a hydrophobic pocket to accommodate the phenol side chain of S0 LQTS site Y111 (Fig. 5D). Long-range electrostatic interactions are also possible between Y111 and the side chains of R174, R181, and K196. This suggests that the Y111C LQTS mutation weakens these hydrophobic and electrostatic interactions, accounting for the severe destabilization of this mutant as documented by NMR (fig. S5 and table S1).

In the C-terminal half of S0, LQTS site L114 makes hydrophobic contacts with Y125 (S1) and V173 (S2) (Fig. 5E), and polar interactions are seen between its backbone C=O and side chains of H126 (S1), R243 (S4), and Q244 (S4). The S0 L114P LQTS mutation, which led to a significant reduction of protein expression in HEK293 cells and failure to express in *E. coli*, would be expected to perturb not only tertiary interactions but also the secondary structure of the S0 helix itself and its

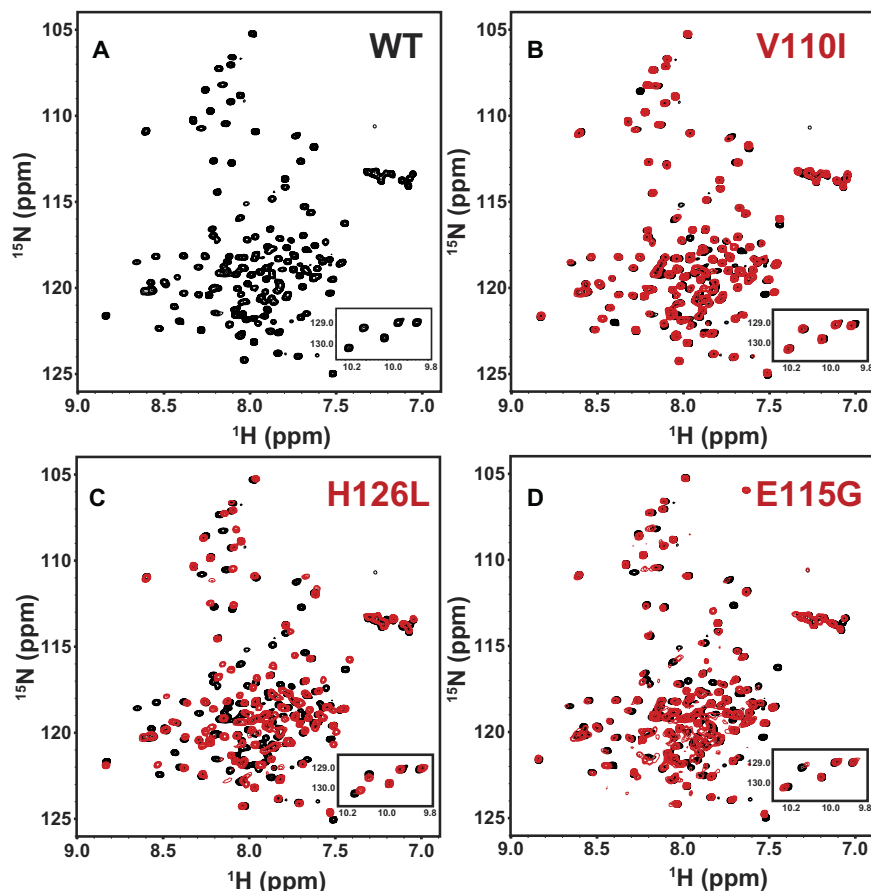


Fig. 4. NMR spectra of WT KCNQ1 and representative mutant forms. $^1\text{H}/^{15}\text{N}$ -TROSY NMR spectra (900 MHz) of the WT KCNQ1 VSD (residues 100 to 249) (A) and representative mutant forms (B to D). ppm, parts per million. The spectrum of each mutant VSD is shown in red, superimposed on the black spectrum of the WT VSD spectrum. Data were collected at 50°C for WT and mutant forms of VSD in LMPG micelles at pH 5.5. The LMPG concentration for all samples was 50 to 80 mM, and the KCNQ1 VSD concentration was 0.3 mM in all samples. (B) The spectrum from the V110I mutant, for which the only changes relative to the WT spectrum are shifts in peak positions. (C) The spectrum from the H126L mutant that is deemed to be moderately destabilized on the basis of a modest degree of line broadening for a number of peaks relative to the corresponding peaks in the WT spectrum. (D) The spectrum from the E115G mutant, which is deemed to be severely destabilized on the basis of extensive peak broadening and even disappearance of a number of peaks.

interaction with the rest of the VSD, thereby disrupting the coordinated network of interactions that S0 makes with various sites in S1, S2, the S2-S3 linker, and S4. Two of the L114-interacting residues, Y125 and H126, are sites in S1 that are subject to VUS mutations, resulting in LOF and mistrafficking (Fig. 5). These residues bridge S0 with sites in S4 known to be critical for voltage-sensing—H240, R243, and Q244 (Fig. 5E) (2)—and therefore could be important not only for the stability but also in the voltage-sensing function of the VSD. The carboxyl chain of S0 LQTS mutation site E115 was seen to frequently form hydrogen bonds with R174 in S2 and K196 in the S2-S3 linker (Fig. 5F) and also forms transient hydrogen bonds with the R243 and R249 in the S4 helix. R174 is an LQTS site and seems to be central to a network of hydrogen bonds that spans all transmembrane helices, connecting sites in S0 (E115) with sites in S2, S3 (D202), and S4 (R243 and Q244).

Finally, S0 and the preceding N-terminal segment were also seen to interact with surrounding membrane lipids and water (see fig. S7). Arginine residues R103 and R109 participated in frequent hydrogen bonding interactions with phosphodiester groups of DMPC. These protein-lipid interactions likely help to anchor the VSD in the membrane

and, thus, represent another mechanism by which S0 contributes to the stability of the VSD.

DISCUSSION

Classifying mechanisms of KCNQ1 dysfunction and LOF

We recently completed a high-throughput electrophysiological investigation of KCNQ1 variants including the 51 mutants studied in this current work (22). Although the focus of the previous study was to illustrate a new and efficient paradigm for linking genotype to function for human ion channels, observations made about the functional consequences of the variants were informative. In particular, a large number of variants (32 of 51) exhibit substantially lower (for example, <65%) peak current density than WT channels, consistent with LOF. Four variants trafficked normally and exhibited normal peak channel currents but were deemed to be dysfunctional because of major alterations in channel $V_{1/2}$ for activation or perturbed deactivation kinetics. Other variants, including 11 of 13 predicted neutral amino acid substitutions, exhibited normal or near-normal function. Among variants associated with LQTS, most (~85%) exhibited LOF traits, but the mechanisms

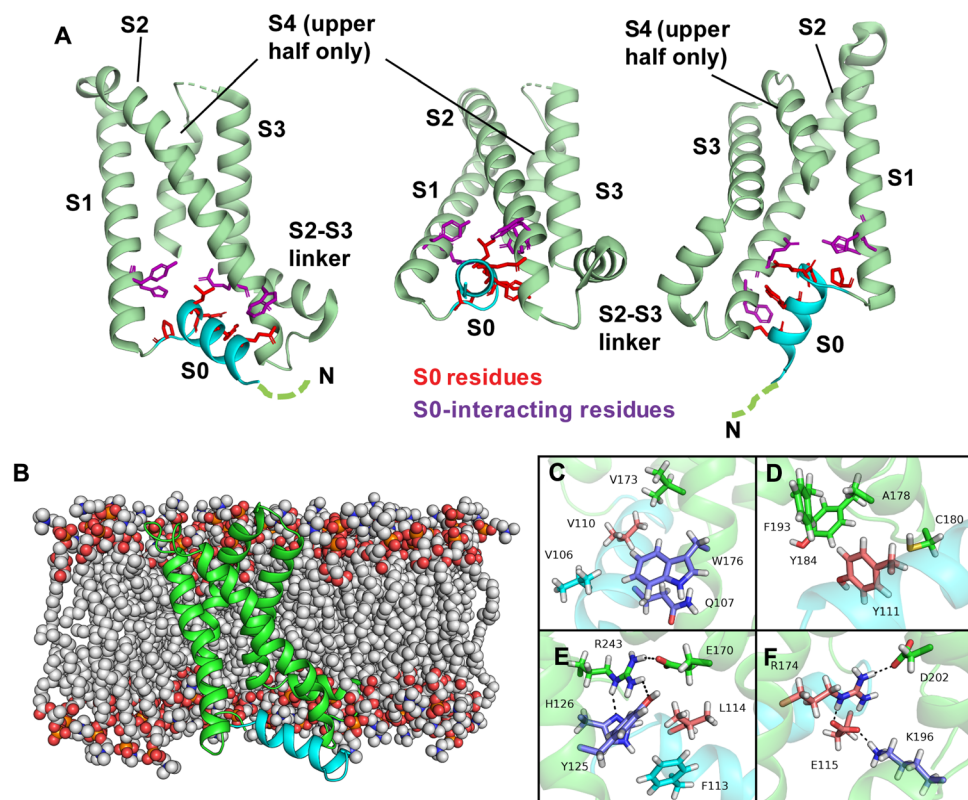


Fig. 5. Structural locations and key interactions involving mutation sites and/or S0 in the KCNQ1 VSD. (A) Three views of the VSD illustrating the locations of the five sites in S0 (red side chains: Q107, Y111, L114, E115, and P117) subject to LQTS mutations that destabilize the VSD, resulting in mistrafficking and degradation of KCNQ1. The side chains for four residues that interact with these S0 residues and that are also subject to destabilizing VUS or LQTS mutations resulting in channel LOF are shown in magenta. The open-state VSD coordinates from the cryo-electron microscopy (EM) structure of KCNQ1 [Protein Data Bank (PDB) ID: 5VMS] were used to generate this figure (23). The V110 LQTS mutation site is also located in S0, but the mutation does not appear to destabilize the protein. (B to F) Results from the MD simulation of the KCNQ1 VSD. (B) Structural model of the WT open-state human VSD in a DMPC bilayer after 500 ns of MD. The VSD is displayed in cartoon representation, with S1-S4 colored pale green and the S0 helix colored cyan. DMPC molecules are depicted as spheres and colored by atom identity: C, gray; O, red; N, blue; P, orange. (C to F) Nonbonded interactions involving sites in S0 and sites contacting S0 for which LQTS and VUS mutations were characterized in this study (see Results). Amino acid side chains are drawn as sticks. LQTS and VUS mutation sites are colored light red and blue, respectively. Residues for which mutations are neutral or have not been characterized in this work are colored gray and green, respectively. Predicted hydrogen bond interactions are indicated by black dotted lines and atoms. The nature of the nonbonded interactions involving S0 is further described in the main body of the text and in table S2.

responsible for this functional impairment were not further explored. Here, we sought to elucidate the mechanisms of channel LOF by quantifying total and cell surface expression levels for WT and mutant forms of KCNQ1.

We observed that 23 of 32 LOF mutants exhibited lower cell surface expression levels ($\leq 65\%$) than WT. Further analysis leads to the conclusion that each KCNQ1 mutant examined in this work can be classified into one of six categories, as summarized below and listed in Table 1.

Class I mutants exhibit normal cell surface expression ($>65\%$ that of WT) but exhibit reduced channel conductance. The mechanism for LOF induced by each such mutation is reduction of channel conductance within otherwise normally folded and trafficked protein. Nine of 32 LOF mutants belong to this class. Additional studies are required to establish exactly how each mutation induces loss of channel function and whether it is possible that there are mechanistic subclasses within this category.

Class II mutants have normal channel properties when properly folded and surface-trafficked but exhibit markedly reduced cell surface expression (only 10 to 65% of WT). Only two variants belong to this class.

Class III mutants reach the cell surface at near-normal levels and display WT-like channel conductance but exhibit significant alterations in the voltage dependence of channel activation and/or altered deactivation kinetics, indicating dysfunctional channel properties. Four mutants fell into this category.

Class IV mutants exhibit low cell surface expression (10 to 65% of WT), with LOF being compounded by the fact that even the population of channels that reaches the cell surface is dysfunctional. Seven mutants belong to this class.

Class V mutants exhibit cell surface levels that are $<10\%$ that of WT. The plasma membrane levels of these mutants are so low that it is not possible to accurately determine whether the very small population of assembled and trafficked channel is functional or not. Fourteen mutants belong to this class.

Class VI mutants exhibit WT-like channel properties, total expression, and surface trafficking. Fifteen of 51 mutants exhibited normal channel trafficking and function. These included 11 of 13 of the predicted benign mutants.

The two “predicted benign” outliers, T118S (class III) and A150V (class I), exhibited properties that caused them to be classified just

Table 1. Classification of KCNQ1 variants.

Classification*	Criteria	Variants†
I	Normal or higher surface trafficking levels, but low peak current density. Dysfunctional channel.	V110I, C122Y, L134P, A150T, A150V, T169M, K218E, I227L, and Q234P
II	Low surface trafficking level but normal or higher channel function for the minority of the population that reaches the plasma membrane.	Q107H and P197L
III	Normal or higher surface levels and peak current density but altered channel $V_{1/2}$ and/or deactivation rate.	H105L‡, R109L, T118S, and I132L
IV	Defective in both channel properties and surface expression levels.	T104I, L131P, E160K, K196T, P197S, L236P, and L236R
V	Severely expression- or trafficking-defective. Current is so low that channel properties cannot be assessed.	Y111C, L114P, E115G, P117L, Y125D, H126L, ΔF167, R174C, R174H, R174L, W176R, G179S, G189A, and R195P
VI (WT-like)	Normal or higher properties in all tested	V100I, A102S, T104S, H105N, H105Y, V106I, V124I, F127L, A128T, V129I, V133I, V135A, V135I, A149V, and V207M

*The 32 mutants in classes I, II, IV, and V are all deemed to be LOF because they exhibit maximal channel conductance $\leq 65\%$ of WT. Surface expression levels were deemed defective if they were $\leq 65\%$ of WT. The four class III mutants exhibit normal maximal peak currents but altered $V_{1/2}$ and/or deactivation rates and are therefore deemed dysfunctional. †The listed mutants are color-coded to indicate their initial classifications before this work: LQTS (red), VUS (blue), or neutral/benign (black). ‡H105L exhibited a hyperpolarizing shift in $V_{1/2}$ for channel activation, R109L exhibited a hyperpolarizing shift in $V_{1/2}$ for activation, T118S exhibited a depolarizing shift in $V_{1/2}$ for activation, and I132L exhibited slowed deactivation.

outside of the range of “normal.” That these two predicted benign mutants exhibited significant dysfunction points to the peril of assuming that sequence variation at a particular protein site between orthologs represents neutral evolutionary drift. The exact functional properties required for the KCNQ1/KCNE1 I_{Ks} channel in the regulation of human heartbeat may be significantly different from the orthologous channel complex in other organisms, such that sequence variation may reflect functionally essential adaptations. Conversely, it must be noted that three LQTS mutants exhibited WT-like properties in our experiments, meaning either that these mutants have defects that we failed to uncover or that they are misclassified.

It seems possible that the personalized treatment of LQTS might, in some cases, benefit from ascertaining which channel LOF mechanism pertains to a given patient. For example, the appropriate therapeutic approach for a class I LQTS patient with KCNQ1 that traffics normally but has defective channel properties is likely to be different from that for a class II patient with KCNQ1 that may be functional if it reaches the plasma membrane but is prone to mistraffic. The tailoring of therapies to varying classes of channel defects has become a reality for certain cystic fibrosis transmembrane regulator (CFTR) mutations that cause cystic fibrosis. For cystic fibrosis, the most common disease-causative mutation is ΔF508 in the CFTR chloride channel. ΔF508 CFTR does not normally traffic to the plasma membrane but, when coaxed to do so by pharmacological chaperones, is then seen to be partially active (32–34). Many others of the hundreds of known CFTR mutants are likely to be trafficking-defective and potentially rescuable by a pharmacological approach (35). On the other hand, some CFTR mutants are known to traffic normally but have dysfunctional channel properties. Drugs that specifically improve the functionality of some such mutants have been developed (32, 33). The feasibility of developing compounds that rescue KCNQ1 mutants based on their specific defects is uncertain. The pharmacological correction of class IV KCNQ1 mutants that are mistrafficking-prone and fail to function, if they do reach the plasma membrane, may be especially difficult.

KCNQ1 misfolding caused by underlying instability as a common LOF mechanism

We observed that the majority (23 of 32) of the LOF mutants examined in this work exhibited much lower (<65%) levels of cell surface expression than WT. This result is reminiscent of the conclusion from studies of the HERG potassium channel that most type 2 LQTS disease mutations in this protein result in trafficking defects (30). These KCNQ1 mutants may also be analogous to Charcot-Marie-Tooth disease (CMTD) mutant forms of the human tetraspan membrane protein peripheral myelin protein 22 (PMP22). Most CMTD mutant forms of PMP22 traffic to the plasma membrane with lower efficiencies than WT PMP22 (36), and it was shown that the efficiency of trafficking correlates linearly with disease severity (37). Moreover, a linear relationship was also observed between the magnitude of energetic destabilization of PMP22 structure and both its intracellular retention (mistrafficking) and disease severity (quantified as patient nerve conduction velocity) (37). That study established mutation-induced destabilization of folded PMP22 as the defect underlying many phenotypes of CMTD.

Here, we have examined whether the same relationship holds between mutation-induced folding destabilization of KCNQ1 and LQTS. Mutants for which structural destabilization is detectable by NMR have been identified. Of 23 KCNQ1 mistrafficking-prone mutants, 17 were determined to be structurally unstable. It is possible that the remaining five mistrafficking mutants are also folding-destabilized, just not to an extent that is evident in their NMR spectra. Significantly, none of the 18 mutants characterized in this work exhibiting WT-like function and trafficking displayed NMR spectral traits that were very different from WT. From these results, we conclude that, at least for the 32 KCNQ1 LOF mutants examined herein, the most common defect that contributes to loss of channel function and LQTS is mutation-induced destabilization of the protein, leading to retention by ER protein folding quality control and ERAD pathway-based degradation by the proteasome. Mistrafficking and degradation via the ERAD pathway have previously been documented for numerous mutant forms of the

HERG channel that result in type 2 LQTS (30). Whether destabilization of the KCNQ1 structure will prove to be the most common mechanism underlying LOF for the hundreds of other known LQTS mutant forms of KCNQ1 remains to be seen. One also wonders whether drug-like small molecules could be developed that can reach and bind nascent KCNQ1 in the ER to stabilize otherwise misfolding-prone channel mutants, leading to restoration of trafficking to the cell surface and, in some cases, channel function. Our work showed that the total expression level for each mutant relative to WT does not always correlate well with the surface trafficking efficiency, with L139P providing a striking example of an exception ($60 \pm 3\%$ total expression relative to WT, but $178 \pm 12\%$ surface trafficking efficiency relative to WT). This indicates complexity in the underlying molecular systems that determine how much nascent channel is degraded, how much evades degradation but fails to surface-traffic, and how much traffics to the plasma membrane. Such complexity could potentially confound a “one compound treats all” approach to correcting trafficking deficiency. The ERAD pathway and related folding and trafficking control systems of the early secretory pathway are indeed known to be formidably complex (38).

PMP22 and KCNQ1 are currently the only two human disease-linked membrane proteins for which the relationship of protein stability to disease mechanism has been definitively established for more than a few select mutations (such as the well-characterized $\Delta F508$ form of the CFTR channel). However, given that other diseases are linked to mutation-induced membrane protein misfolding, such as retinitis pigmentosa (rhodopsin), Pelizaeus-Merzbacher disease (proteolipid protein), and diabetes insipidus (vasopressin V2 receptor), it is likely that mutation-induced destabilization is also a trigger for the disease-causative intracellular retention and/or degradation of these proteins. There is a pressing need to develop general methods to quantitatively compare the stabilities of WT and disease mutant forms of these proteins. It is also interesting to note that some of the mutation sites associated with the destabilization of KCNQ1 correspond via homology to known disease mutation sites in other voltage-gated ion channels (39–41), including a number of KCNQ2 and KCNQ3 sites for which mutations are associated with benign familial neonatal seizures and epileptic encephalopathy (see <http://www.hgmd.cf.ac.uk>). This suggests that mutation-induced destabilization of protein folding is likely a very common underlying mechanism for many other channelopathies.

Stabilization of the S0 helix by the KCNQ1 VSD

The S0 segment found in many voltage-gated channels has previously received little attention as to its roles in VSD structure and function [note that the S0 segment in KCNQ1 and other Shaker-type channels should not be confused with the transmembrane S0 helix in BK (Big Potassium) channels]. Our results reveal a critical role for this widely conserved structural element. Of the 17 KCNQ1 mutants observed in this work to be significantly folding-destabilized, 5 involve LQTS mutations at sites located in S0 (Q107H, Y111C, L114P, E115G, and P117L; see fig. S1 and Fig. 5). We note that S0 mutants Y111C, L114P, and P117L have previously been identified as trafficking-defective (40, 42). Another seven mistrafficking-prone mutants (Y125D, H126L, R174C, R174H, R174L, W176R, and G179S; Fig. 5) involve sites in S1 or S2 that interact with the five LQTS sites in S0. MD simulations illuminated the role of S0 as a central scaffolding element that is engaged in a dense network of interactions with other VSD segments, even the functionally critical S4 (Fig. 5). This is further supported by the observation that residues in S0 move in a concerted and correlated fashion with residues in S2 and S4 (see fig. S8).

Combined, these observations indicate that S0 contributes to organizing and stabilizing the structure of the VSD.

S0 segments are present in many other voltage-gated channels and also in the VSD-like regulatory domain of transient receptor potential channels (23, 43–47). As we observed for KCNQ1, disease-causing mutations are sometimes found in the S0 segments of these other channels. For example, each of the four distinct S0 segments in the human voltage-gated sodium channel SCN5A ($\text{Na}_v1.5$) has at least one known LQTS and/or Brugada syndrome-associated mutation [11 in total; see www.uniprot.org/uniprot/Q14524 (23)]. It seems very likely that the critical role for S0 documented in this work for KCNQ1 may extend to other voltage-gated ion channels.

CONCLUSIONS

This study confirms the value of conducting studies of the trafficking and stability of KCNQ1 variants, studies that complement EP functional studies. Not only is significant additional mechanistic information provided regarding the loss of channel function for many variants, but fundamental new insights into KCNQ1 channel structure-function-stability relationships can be gleaned (that is, recognition of the importance of S0 in VSD structure and stability). This work also highlights the importance of membrane protein destabilization as a potential disease mechanism. The results of this work could conceivably affect future personalized medical decisions for patients with one of the KCNQ1 mutants characterized in this work. Moreover, the results may be used to help train computational algorithms being developed to predict channel functionality and disease outcomes for patients that harbor KCNQ1 VUS.

MATERIALS AND METHODS

Cloning

The *c-myc*-tagged human KCNQ1 DNA (GenBank accession number AF000571), a gift from D. Roden of Vanderbilt University (24), was subcloned into a pIRES2-enhanced green fluorescent protein (EGFP) vector. The *c-myc* tag (EQKLISEEDL) was introduced into the extracellular S1-S2 linker between Glu¹⁴⁶ and Gln¹⁴⁷. The VSD, spanning KCNQ1 residues 100 to 249, was cloned into a pET16b vector with an N-terminal His tag (MHHHHHHG-). Human KCNE1 (L28168) was subcloned into a pcDNA3.1(+) vector. Mutants were generated by QuikChange site-directed mutagenesis using WT *myc-KCNQ1* or *KCNQ1* VSD complementary DNA as the template and verified by sequencing to confirm the presence of the desired mutation(s).

Cell culture and transfection

HEK293 cells were purchased from the American Type Culture Collection. Cells were cultured in Dulbecco's modified Eagle's medium supplemented with 10% fetal bovine serum (FBS), 10 mM HEPES, penicillin (100 U/ml), and streptomycin (100 $\mu\text{g}/\text{ml}$) at 37°C in a humidified atmosphere with 5% CO_2 . HEK293 cells were plated into six-well plates and transfected with 0.5 μg WT or mutant *myc-KCNQ1* per well at 30 to 50% confluence using FuGENE 6 transfection reagent (Promega). When WT and mutant *myc-KCNQ1* were cotransfected, the WT/mutant or WT/pIRES2-EGFP vector ratio was 1:1 and total DNA was 0.5 μg . Approximately 48 hours later, cells were prepared for flow cytometry measurements. To assess the effect of proteasome inhibitor on *myc-KCNQ1* expression, we treated cells starting 1 day after transfection with 25 μM MG132 or 0.1% dimethyl sulfoxide

(DMSO) (control) for 20 hours before quantitating KCNQ1 protein levels.

Flow cytometry

On the day of the experiment, cells were placed on ice and washed once with ice-cold phosphate-buffered saline flow cytometry buffer (PBS-FC) containing 25 mM Hepes and 0.1% NaN₃, pH 7.4. Cells were detached in 0.5 mM EDTA in PBS-FC and precipitated by centrifugation at 500g for 5 min. As previously described (37), cells were then permeabilized and stained using the FIX & PERM Kit (Thermo Fisher Scientific) following the manufacturer's instructions. Briefly, cells were incubated with 100 μ l of PE-conjugated myc-tag (9B11) mouse monoclonal antibody (Cell Signaling Technology) (1:100 dilution in PBS-FC containing 5% FBS) for 30 min in the dark at room temperature. Fixation medium (100 μ l) was then added, and cells were incubated for 15 min to be fixed. Cells were then washed once with PBS-FC containing 5% FBS and incubated with Alexa Fluor 647-conjugated myc-tag (9B11) mouse monoclonal antibody (Cell Signaling Technology) (1:100 dilution in permeabilization medium) for 30 min in the dark at room temperature. Cells were rinsed once, and fluorescence signals were then measured using a FACS Canto II flow cytometer (BD Biosciences). Cells expressing WT myc-KCNQ1 were permeabilized and stained with either PE- or Alexa Fluor 647-conjugated antibody to normalize the two fluorescence signals. For the proteasome inhibitor study, cells were fixed and permeabilized (this step was omitted for measuring the surface expression) and then stained with myc-tag (9B11) mouse monoclonal antibody (Cell Signaling Technology) (1:500 dilution in PBS-FC containing 5% FBS) for 30 min at room temperature. Cells were then washed and stained with anti-mouse Alexa Fluor 647 antibody (Cell Signaling Technology) (1:1000 dilution in PBS-FC containing 5% FBS) for 30 min at room temperature in the dark. Single cells expressing myc-KCNQ1 were selected by gating on GFP-positive cells. Fluorescence of cells transfected with the empty vector was used to account for background staining. The expression levels of mutants were calculated as a percentage of the WT channel. The mean and the SEM were calculated from at least three independent experiments. Data were analyzed using GraphPad 6.0 software. The statistical significance of the differences between WT and mutants or between DMSO- and MG132-treated cells was determined by Student's *t* test.

Overexpression and purification of the VSD in *E. coli*

WT and mutant forms of the KCNQ1 VSD were expressed and purified essentially as previously described (48). Briefly, KCNQ1 VSD was expressed in Rosetta/C43(DE3) cells and cultured in ¹⁵N-labeled M9 minimal medium. Cells were induced by 1 mM isopropyl- β -D-thiogalactopyranoside for 24 hours at room temperature and then harvested. Each gram of cells was suspended in 20 ml of lysis buffer [75 mM Tris-HCl, 300 mM NaCl, and 0.2 mM EDTA (pH 7.8)] with 5 mM Mg(Ac)₂, phenylmethylsulfonyl fluoride (0.2 mg/ml), deoxyribonuclease (0.02 mg/ml), ribonuclease (0.02 mg/ml), and lysozyme (0.2 mg/ml) and was tumbled for about 30 min. The lysate was probe-sonicated at 4°C for 5 min with 5-s pulses separated by 5 s. The inclusion body was isolated by centrifugation at 20 kg for 20 min and washed once in lysis buffer. The inclusion body was then solubilized in buffer A [40 mM Hepes and 300 mM NaCl (pH 7.5)] containing 0.5% dodecylphosphocholine (DPC) (Anatrace) and 2 mM tris(2-carboxyethyl)phosphine (TCEP) overnight at 4°C. Insoluble debris was removed by centrifugation at 20 kg for 20 min, and the supernatant was incubated with Ni(II)-NTA Superflow resin (Qiagen) for at least 1 hour at 4°C. The resin was

then packed into a gravity-flow column and washed with 10 bed volumes of buffer A containing 0.5% DPC and 2 mM TCEP. Impurities were removed by extensive washing with 12 bed volumes of buffer A containing 0.5% DPC, 2 mM TCEP, and 60 mM imidazole (pH 7.8). DPC on the column was exchanged with LMPG (Anatrace) by washing the column with 10 bed volumes of buffer A containing 0.05% LMPG and 2 mM TCEP. The KCNQ1 VSD was then eluted in buffer A containing 0.2% LMPG, 2 mM TCEP, and 500 mM imidazole (pH 7.8) until A₂₈₀ (as monitored continuously) returned to the baseline level (typically 3 bed volumes).

NMR spectroscopy

The KCNQ1 VSD (residues 100 to 249) concentration was determined by A₂₈₀ using an extinction coefficient of 34,950 M⁻¹ cm⁻¹. When needed, more LMPG was added to samples to adjust the ratio of LMPG micelles to protein molecules to 3 to 5. The eluted protein sample was concentrated 10-fold using an Amicon Ultra centrifugal filter cartridge (30,000 molecular weight cutoff). The sample was diluted with NMR buffer [50 mM MES, 0.5 mM EDTA, 2 mM TCEP, and 0.2 mM LMPG (its critical micelle concentration) (pH 5.5)] to the initial elution volume and was again concentrated 10-fold. The process was repeated a total of three times to ensure efficient buffer exchange. The 200 μ l of NMR sample containing 0.3 mM KCNQ1 VSD, 50 to 80 mM LMPG, and 5% D₂O was then transferred into a 3-mm NMR tube. The 2D ¹H/¹⁵N-TROSY experiment was conducted using the standard Bruker pulse sequence. All NMR data were collected at 50°C on a Bruker 800- or 900-MHz NMR spectrometer.

Homology modeling of the KCNQ1 VSD structure

A structural model of the KCNQ1 VSD (residues 100 to 249) was generated using the protein structure prediction software package Rosetta (version 3.8) (49) based on the cryo-EM structure of *Xenopus* KCNQ1 (PDB ID: 5VMS) (23), and sequence alignment was generated with ClustalW (50). Four thousand models of KCNQ1 VSD were assembled through comparative modeling (51) using the Rosetta Membrane energy function (52). Gaps in the threaded model resulting from unresolved regions in the template structure were reconstructed by fragment insertion and cyclic coordinate descent loop building (53). All models underwent side-chain repacking and all-atom refinement while applying a low constraint to the initial coordinates. Models were clustered on the basis of root mean square deviation (RMSD). The lowest-scoring model of the largest cluster was considered the representative model. Its Ca RMSD compared to the *Xenopus* KCNQ1 VSD structure was 2.3 Å. MolProbity analysis of the representative model reported an overall score of 1.34 (98th percentile), a clash score of 2.02 (99th percentile), 140 (95.0%) residues in favored regions of the Ramachandran plot, all residues in allowed regions, 126 (98.4%) favored rotamers, no poor rotamers, and no C β deviations or bad backbone angles.

MD simulation of KCNQ1 VSD in a lipid bilayer

An MD simulation of the KCNQ1 VSD was performed in an explicit DMPC bilayer at 313 K using Amber16 (54) and the Lipid14 force field (55). Three independent trajectories, each having a total length of 500 ns but starting with different input models, were computed. Our ensemble of KCNQ1 VSD homology models was clustered using a hierarchical full-linkage clustering algorithm (56), and the centroids of the three largest clusters were chosen as starting coordinates. The coordinates of each input model were aligned with the membrane

normal using the PPM web server (57). A complete model of the KCNQ1 VSD in a DMPC bilayer (110 lipids per leaflet) was prepared with the membrane builder tool of the CHARMM-GUI website (58). A TIP3P water layer of 20 Å was included, and Cl⁻ ions were added to neutralize the charge of the system. Each bilayer system was first minimized for 15,000 steps using steepest descent followed by 15,000 steps of conjugate gradient minimization. With the KCNQ1 VSD restrained to its starting coordinates, the lipid and water were heated to 50 K over 1000 steps with a step size of 1 fs using constant boundary conditions and Langevin dynamics with a rapid collision frequency of 10,000 ps⁻¹. The system was then heated to 100 K over 50,000 steps with constant volume dynamics and the collision frequency set to 1000 ps⁻¹ and, finally, to 313 K over 100,000 steps with constant pressure dynamics and anisotropic pressure scaling turned on. Positional restraints on the KCNQ1 VSD were then gradually removed over 500 ps, and the system was equilibrated for another 5 ns at 313 K. Production MD was conducted for 500 ns using a step size of 1 fs, constant pressure periodic boundary conditions, anisotropic pressure scaling, and Langevin dynamics. MD trajectories were analyzed using CPPTRAJ (version 15.0) (59) and VMD (visual molecular dynamics; version 1.9) (60).

SUPPLEMENTARY MATERIALS

Supplementary material for this article is available at <http://advances.sciencemag.org/cgi/content/full/4/3/eaar2631/DC1>

- fig. S1. Locations of the human KCNQ1 mutation examined in this work.
 fig. S2. Fluorimetric cell flow cytometry assay used to determine total and surface protein expression levels.
 fig. S3. Surface trafficking efficiency for each mutant juxtaposed with KCNQ1 peak current density.
 fig. S4. Effect of coexpression of KCNE1 with KCNQ1 on total surface expression levels of KCNQ1.
 fig. S5. ¹H/¹⁵N-TROSY NMR spectra (900 MHz) of KCNQ1 mutants (red) superimposed on the spectrum of WT KCNQ1 (black).
 fig. S6. Results from MD trajectories.
 fig. S7. Hydrogen bond interactions of the KCNQ1 VSD with solvent are observed during MD simulation.
 fig. S8. Correlation plot of residue motions calculated from KCNQ1 VSD MD simulations.
 table S1. Functional and trafficking results for 51 human KCNQ1 mutants.
 table S2. List of nonbonded interactions of LQTS1 and VUS mutation sites in S0 and S0-contacting regions observed during MD simulation of the KCNQ1 VSD.

REFERENCES AND NOTES

- G. W. Abbott, KCNE1 and KCNE3: The yin and yang of voltage-gated K⁺ channel regulation. *Gene* **576**, 1–13 (2016).
- J. Cui, Voltage-dependent gating: Novel insights from KCNQ1 channels. *Biophys. J.* **110**, 14–25 (2016).
- T. Jespersen, M. Grunnet, S.-P. Olesen, The KCNQ1 potassium channel: From gene to physiological function. *Physiology* **20**, 408–416 (2005).
- S. I. Liin, R. Barro-Soria, H. P. Larsson, The KCNQ1 channel—Remarkable flexibility in gating allows for functional versatility. *J. Physiol.* **593**, 2605–2615 (2015).
- K. Nakajo, Y. Kubo, KCNQ1 channel modulation by KCNE proteins via the voltage-sensing domain. *J. Physiol.* **593**, 2617–2625 (2015).
- W. Wu, M. C. Sanguinetti, Molecular basis of cardiac delayed rectifier potassium channel function and pharmacology. *Card. Electrophysiol. Clin.* **8**, 275–284 (2016).
- J. Wu, W. G. Ding, M. Horie, Molecular pathogenesis of long QT syndrome type 1. *J. Arrhythm. Clin. Electrophysiol.* **32**, 381–388 (2016).
- T. Zhang, A. Moss, P. Cong, M. Pan, B. Chang, L. Zheng, Q. Fang, W. Zareba, J. Robinson, C. Lin, Z. Li, J. Wei, Q. Zeng; Long QT International Registry Investigators; HVP-China Investigators, M. Qi, LQTS gene LOVD database. *Hum. Mutat.* **31**, E1801–E1810 (2010).
- S. M. Harrison, E. R. Riggs, D. R. Maglott, J. M. Lee, D. R. Azzariti, A. Niehaus, E. M. Ramos, C. L. Martin, M. J. Landrum, H. L. Rehm, Using ClinVar as a resource to support variant interpretation. *Curr. Protoc. Hum. Genet.* **89**, 8.16.1–8.16.23 (2016).
- P. D. Stenson, E. V. Ball, M. Mort, A. D. Phillips, K. Shaw, D. N. Cooper, The Human Gene Mutation Database (HGMD) and its exploitation in the fields of personalized genomics and molecular evolution. *Curr. Protoc. Bioinformatics* **Chapter 1**, Unit 1.13 (2012).
- M. Dvir, A. Peretz, Y. Haitin, B. Attali, Recent molecular insights from mutated I_{Ks} channels in cardiac arrhythmia. *Curr. Opin. Pharmacol.* **15**, 74–82 (2014).
- J. Eldstrom, Z. Wang, D. Werry, N. Wong, D. Fedida, Microscopic mechanisms for long QT syndrome type 1 revealed by single-channel analysis of I_{Ks} with S3 domain mutations in KCNQ1. *Heart Rhythm* **12**, 386–394 (2015).
- L. Restier, L. Cheng, M. C. Sanguinetti, Mechanisms by which atrial fibrillation-associated mutations in the S1 domain of KCNQ1 slow deactivation of I_{Ks} channels. *J. Physiol.* **586**, 4179–4191 (2008).
- T. Yang, S. K. Chung, W. Zhang, J. G. Mullins, C. H. McCulley, J. Crawford, J. MacCormick, C. A. Eddy, A. N. Shelling, J. K. French, P. Yang, J. R. Skinner, D. M. Roden, M. I. Rees, Biophysical properties of 9 KCNQ1 mutations associated with long-QT syndrome. *Circ. Arrhythm. Electrophysiol.* **2**, 417–426 (2009).
- G. Seebohm, N. Strutz-Seebohm, O. N. Ureche, U. Henrion, R. Baltaev, A. F. Mack, G. Korniyuk, K. Steinke, D. Tapken, A. Pfeufer, S. Käbb, C. Bucci, B. Attali, J. Merot, J. M. Tavare, U. C. Hoppe, M. C. Sanguinetti, F. Lang, Long QT syndrome-associated mutations in KCNQ1 and KCNE1 subunits disrupt normal endosomal recycling of I_{Ks} channels. *Circ. Res.* **103**, 1451–1457 (2008).
- B. Li, J. L. Mendenhall, B. M. Kroncke, K. C. Taylor, H. Huang, D. K. Smith, C. G. Vanoye, J. D. Blume, A. L. George Jr., C. R. Sanders, J. Meiler, Predicting the functional impact of KCNQ1 variants of unknown significance. *Circ. Cardiovasc. Genet.* **10**, e001754 (2017).
- M. J. Ackerman, Genetic purgatory and the cardiac channelopathies: Exposing the variants of uncertain/unknown significance issue. *Heart Rhythm* **12**, 2325–2331 (2015).
- J. R. Giudicessi, J. D. Kapplinger, D. J. Tester, M. Alders, B. A. Salisbury, A. A. Wilde, M. J. Ackerman, Phylogenetic and physicochemical analyses enhance the classification of rare nonsynonymous single nucleotide variants in type 1 and 2 long-QT syndrome. *Circ. Cardiovasc. Genet.* **5**, 519–528 (2012).
- J. D. Kapplinger, A. S. Tseng, B. A. Salisbury, D. J. Tester, T. E. Callis, M. Alders, A. A. Wilde, M. J. Ackerman, Enhancing the predictive power of mutations in the C-terminus of the KCNQ1-encoded Kv7.1 voltage-gated potassium channel. *J. Cardiovasc. Transl. Res.* **8**, 187–197 (2015).
- I. U. S. Leong, A. Stuckey, D. Lai, J. R. Skinner, D. R. Love, Assessment of the predictive accuracy of five in silico prediction tools, alone or in combination, and two metaservers to classify long QT syndrome gene mutations. *BMC Med. Genet.* **16**, 34 (2015).
- S. Richards, N. Aziz, S. Bale, D. Bick, S. Das, J. Gastier-Foster, W. W. Grody, M. Hegde, E. Lyon, E. Spector, K. Voelkerding, H. L. Rehm; ACMG Laboratory Quality Assurance Committee, Standards and guidelines for the interpretation of sequence variants: A joint consensus recommendation of the American College of Medical Genetics and Genomics and the Association for Molecular Pathology. *Genet. Med.* **17**, 405–424 (2015).
- C. Vanoye, R. Desai, K. Fabre, F. Potet, J.-M. DeKeyser, D. Macaya, J. Meiler, C. Sanders, A. George, High throughput functional evaluation of KCNQ1 decrypts variants of unknown significance. www.biorxiv.org/content/early/2017/11/21/223206.article-info, doi.org/10.1101/223206 (2017).
- J. Sun, R. MacKinnon, Cryo-EM structure of a KCNQ1/CaM complex reveals insights into congenital long QT syndrome. *Cell* **169**, 1042–1050.e9 (2017).
- H. Kanki, S. Kupersmidt, T. Yang, S. Wells, D. M. Roden, A structural requirement for processing the cardiac K⁺ channel KCNQ1. *J. Biol. Chem.* **279**, 33976–33983 (2004).
- J.-P. David, M. N. Andersen, S.-P. Olesen, H. B. Rasmussen, N. Schmitt, Trafficking of the I_{Ks}-complex in MDCK cells: Site of subunit assembly and determinants of polarized localization. *Traffic* **14**, 399–411 (2013).
- V. A. Kanda, G. W. Abbott, KCNE regulation of K⁺ channel trafficking—A Sisyphus task? *Front. Physiol.* **3**, 231 (2012).
- C. G. Vanoye, R. C. Welch, C. Tian, C. R. Sanders, A. L. George Jr., KCNQ1/KCNE1 assembly, co-translation not required. *Channels (Austin)* **4**, 108–114 (2010).
- K. McCaffrey, I. Braakman, Protein quality control at the endoplasmic reticulum. *Essays Biochem.* **60**, 227–235 (2016).
- R. Riek, K. Pervushin, K. Wüthrich, TROSY and CRINEPT: NMR with large molecular and supramolecular structures in solution. *Trends Biochem. Sci.* **25**, 462–468 (2000).
- J. L. Smith, C. L. Anderson, D. E. Burgess, C. S. Elayi, C. T. January, B. P. Delisle, Molecular pathogenesis of long QT syndrome type 2. *J. Arrhythm.* **32**, 373–380 (2016).
- C. Altier, A. Garcia-Caballero, B. Simms, H. You, L. Chen, J. Walcher, H. W. Tedford, T. Hermosilla, G. W. Zamponi, The Cavβ subunit prevents RFP2-mediated ubiquitination and proteasomal degradation of L-type channels. *Nat. Neurosci.* **14**, 173–180 (2011).
- I. Fajac, K. De Boeck, New horizons for cystic fibrosis treatment. *Pharmacol. Ther.* **170**, 205–211 (2017).
- K. Harman, R. Dobra, J. C. Davies, Disease-modifying drug therapy in cystic fibrosis. *Paediatr. Respir. Rev.* S1526-0542(17)30031-3 (2017).
- G. L. Lukacs, A. S. Verkman, CFTR: Folding, misfolding and correcting the ΔF508 conformational defect. *Trends Mol. Med.* **18**, 81–91 (2012).

35. Y. Wang, J. A. Wrennall, Z. Cai, H. Li, D. N. Sheppard, Understanding how cystic fibrosis mutations disrupt CFTR function: From single molecules to animal models. *Int. J. Biochem. Cell Biol.* **52**, 47–57 (2014).
36. R. Naef, U. Suter, Impaired intracellular trafficking is a common disease mechanism of PMP22 point mutations in peripheral neuropathies. *Neurobiol. Dis.* **6**, 1–14 (1999).
37. J. P. Schleich, M. Narayan, C. Alford, K. F. Mittendorf, B. D. Carter, J. Li, C. R. Sanders, Conformational stability and pathogenic misfolding of the integral membrane protein PMP22. *J. Am. Chem. Soc.* **137**, 8758–8768 (2015).
38. J. A. Olzmann, R. R. Kopito, J. C. Christianson, The mammalian endoplasmic reticulum-associated degradation system. *Cold Spring Harb. Perspect. Biol.* **5**, a013185 (2013).
39. J. K. Myers, L. A. Beihoffer, C. R. Sanders, Phenotology of disease-linked proteins. *Hum. Mutat.* **25**, 90–97 (2005).
40. S. Dahimene, S. Alcoléa, P. Naud, P. Jourdon, D. Escande, R. Brasseur, A. Thomas, I. Baró, J. Mérot, The N-terminal juxtamembranous domain of KCNQ1 is critical for channel surface expression: Implications in the Romano-Ward LQT1 syndrome. *Circ. Res.* **99**, 1076–1083 (2006).
41. F. Zara, N. Specchio, P. Striano, A. Robbiano, E. Gennaro, R. Paravidino, N. Vanni, F. Beccaria, G. Capovilla, A. Bianchi, L. Caffi, V. Cardilli, F. Darra, B. D. Bernardina, L. Fusco, R. Gaggero, L. Giordano, R. Guerrini, G. Incorpora, M. Mastrangelo, L. Spaccini, A. M. Laverda, M. Vecchi, F. Vanadia, P. Veggiotti, M. Viri, G. Occhi, M. Budetta, M. Tagliatela, D. A. Coviello, F. Vigeveno, C. Minetti, Genetic testing in benign familial epilepsies of the first year of life: Clinical and diagnostic significance. *Epilepsia* **54**, 425–436 (2013).
42. D. Peroz, S. Dahimene, I. Baró, G. Loussouarn, J. Mérot, LQT1-associated mutations increase KCNQ1 proteasomal degradation independently of Derlin-1. *J. Biol. Chem.* **284**, 5250–5256 (2009).
43. J. Guo, W. Zeng, Q. Chen, C. Lee, L. Chen, Y. Yang, C. Cang, D. Ren, Y. Jiang, Structure of the voltage-gated two-pore channel TPC1 from *Arabidopsis thaliana*. *Nature* **531**, 196–201 (2016).
44. M. Liao, E. Cao, D. Julius, Y. Cheng, Structure of the TRPV1 ion channel determined by electron cryo-microscopy. *Nature* **504**, 107–112 (2013).
45. S. B. Long, X. Tao, E. B. Campbell, R. MacKinnon, Atomic structure of a voltage-dependent K⁺ channel in a lipid membrane-like environment. *Nature* **450**, 376–382 (2007).
46. J. Payandeh, T. Scheuer, N. Zheng, W. A. Catterall, The crystal structure of a voltage-gated sodium channel. *Nature* **475**, 353–358 (2011).
47. J. Wu, Z. Yan, Z. Li, X. Qian, S. Lu, M. Dong, Q. Zhou, N. Yan, Structure of the voltage-gated calcium channel Ca_v1.1 at 3.6 Å resolution. *Nature* **537**, 191–196 (2016).
48. D. G. Peng, J. H. Kim, B. M. Kroncke, C. L. Law, Y. Xia, K. D. Droege, W. D. Van Horn, C. G. Vanoye, C. R. Sanders, Purification and structural study of the voltage-sensor domain of the human KCNQ1 potassium ion channel. *Biochemistry* **53**, 2032–2042 (2014).
49. A. Leaver-Fay, M. Tyka, S. M. Lewis, OF Lange, J. Thompson, R. Jacak, K. Kaufman, P. D. Renfrew, C. A. Smith, W. Sheffler, I. W. Davis, S. Cooper, A. Treuille, D. J. Mandell, F. Richter, Y. E. Ban, S. J. Fleishman, J. E. Corn, D. E. Kim, S. Lyskov, M. Berrondo, S. Mentzer, Z. Popović, J. J. Havranek, J. Karanicolas, R. Das, J. Meiler, T. Kortemme, J. J. Gray, B. Kuhlman, D. Baker, P. Bradley, ROSETTA3: An object-oriented software suite for the simulation and design of macromolecules. *Methods Enzymol.* **487**, 545–574 (2011).
50. M. A. Larkin, G. Blackshields, N. P. Brown, R. Chenna, P. A. McGettigan, H. McWilliam, F. Valentin, I. M. Wallace, A. Wilm, R. Lopez, J. D. Thompson, T. J. Gibson, D. G. Higgins, Clustal W and Clustal X version 2.0. *Bioinformatics* **23**, 2947–2948 (2007).
51. Y. F. Song, F. DiMaio, R. Y.-R. Wang, D. Kim, C. Miles, T. Brunette, J. Thompson, D. Baker, High-resolution comparative modeling with RosettaCM. *Structure* **21**, 1735–1742 (2013).
52. P. Barth, J. Schonbrun, D. Baker, Toward high-resolution prediction and design of transmembrane helical protein structures. *Proc. Natl. Acad. Sci. U.S.A.* **104**, 15682–15687 (2007).
53. A. A. Canutescu, R. L. Dunbrack Jr., Cyclic coordinate descent: A robotics algorithm for protein loop closure. *Protein Sci.* **12**, 963–972 (2003).
54. D. A. Case, T. E. Cheatham III, T. Darden, H. Gohlke, R. Luo, K. M. Merz Jr., A. Onufriev, C. Simmerling, B. Wang, R. J. Woods, The Amber biomolecular simulation programs. *J. Comput. Chem.* **26**, 1668–1688 (2005).
55. C. J. Dickson, B. D. Madej, A. A. Skjevik, R. M. Betz, K. Teigen, I. R. Gould, R. C. Walker, Lipid14: The Amber lipid force field. *J. Chem. Theory Comput.* **10**, 865–879 (2014).
56. I. M. Overton, C. A. van Niekerk, L. G. Carter, A. Dawson, D. M. Martin, S. Cameron, S. A. McMahon, M. F. White, W. N. Hunter, J. H. Naismith, G. J. Barton, TarO: A target optimisation system for structural biology. *Nucleic Acids Res.* **36**, W190–196 (2008).
57. M. A. Lomize, I. D. Pogozheva, H. Joo, H. I. Mosberg, A. L. Lomize, OPM database and PPM web server: Resources for positioning of proteins in membranes. *Nucleic Acids Res.* **40**, D370–D376 (2012).
58. E. L. Wu, X. Cheng, S. Jo, H. Rui, K. C. Song, E. M. Dávila-Contreras, Y. Qi, J. Lee, V. Monje-Galvan, R. M. Venable, J. B. Klauda, W. Im, CHARMM-GUI Membrane Builder toward realistic biological membrane simulations. *J. Comput. Chem.* **35**, 1997–2004 (2014).
59. D. R. Roe, T. E. Cheatham III, PTRAJ and CPPTRAJ: Software for processing and analysis of molecular dynamics trajectory data. *J. Chem. Theory Comput.* **9**, 3084–3095 (2013).
60. W. Humphrey, A. Dalke, K. Schulten, VMD: Visual molecular dynamics. *J. Mol. Graph.* **14**, 33–38 (1996).

Acknowledgments: We thank R. Desai and K. Fabre for technical assistance and B. Kroncke for helpful discussion throughout this project. **Funding:** This work was supported by U.S. NIH grant RO1 HL122010. K.C.T. was supported by NIH fellowship F32 GM117770 and NIH training grant T32 NS00749. G.K. was supported by a fellowship from the German Research Foundation (KU 3510/1-1). The NMR instrumentation used in this work was supported by NIH S10 RR026677 and NSF DBI-0922862, whereas the computational resources were supported by NIH S10 OD020154 and NIH S10 RR031634. **Author contributions:** H.H., G.K., J.A.S., K.C.T., A.M.D., and A.H. conducted the experiments and calculations. H.H., C.G.V., A.L.G., and C.R.S. wrote the paper with input from all authors. J.M., C.G.V., A.L.G., and C.R.S. conceived this work and directed the approaches used. All authors participated in data analysis.

Competing interests: A.L.G. serves on the Scientific Advisory Boards of Amgen Inc. and Otsuka Pharmaceuticals. All other authors declare that they have no competing interests.

Data and materials availability: All data needed to evaluate the conclusions in the paper are present in the paper and/or the Supplementary Materials. Additional data related to this paper may be requested from the authors. Requests for materials and for the reagents and/or expression vectors described in this work should be addressed to C.R.S. (chuck.sanders@vanderbilt.edu). Reagents and expression vectors described in this work can be provided by C.R.S. (Vanderbilt University) pending scientific review and a completed material transfer agreement.

Submitted 19 October 2017

Accepted 2 February 2018

Published 7 March 2018

10.1126/sciadv.aar2631

Citation: H. Huang, G. Kuenze, J. A. Smith, K. C. Taylor, A. M. Duran, A. Hadziselimovic, J. Meiler, C. G. Vanoye, A. L. George Jr., C. R. Sanders Mechanisms of KCNQ1 channel dysfunction in long QT syndrome involving voltage sensor domain mutations. *Sci. Adv.* **4**, eaar2631 (2018).

Mechanisms of KCNQ1 channel dysfunction in long QT syndrome involving voltage sensor domain mutations

Hui Huang, Georg Kuenze, Jarrod A. Smith, Keenan C. Taylor, Amanda M. Duran, Arina Hadziselimovic, Jens Meiler, Carlos G. Vanoye, Alfred L. George, Jr and Charles R. Sanders

Sci Adv 4 (3), eaar2631.
DOI: 10.1126/sciadv.aar2631

ARTICLE TOOLS

<http://advances.sciencemag.org/content/4/3/eaar2631>

SUPPLEMENTARY MATERIALS

<http://advances.sciencemag.org/content/suppl/2018/03/05/4.3.eaar2631.DC1>

REFERENCES

This article cites 58 articles, 10 of which you can access for free
<http://advances.sciencemag.org/content/4/3/eaar2631#BIBL>

PERMISSIONS

<http://www.sciencemag.org/help/reprints-and-permissions>

Use of this article is subject to the [Terms of Service](#)

Science Advances (ISSN 2375-2548) is published by the American Association for the Advancement of Science, 1200 New York Avenue NW, Washington, DC 20005. 2017 © The Authors, some rights reserved; exclusive licensee American Association for the Advancement of Science. No claim to original U.S. Government Works. The title *Science Advances* is a registered trademark of AAAS.